J Solid State Electrochem (2006) 10: 700–707
DOI 10.1007/s10008-006-0114-2

ORIGINAL PAPER

Eimutis Juzeliūnas · Yu Pei Ma · John P. Wikswo

Magnetometric corrosion sensing under hydrodynamic conditions

Received: 30 May 2005 / Accepted: 9 November 2005 / Published online: 5 May 2006

Abstract SQUID (Superconducting QUantum Interference Device) magnetometer operating in liquid helium with a special resolution of ca. 1 mm was used to study the magnetic fields produced by corrosion reactions under electrolyte flow conditions. Macroscopic magnetic field images were obtained on AA 2024 samples corroding in naturally aerated and oxygen-saturated NaCl solutions and 0.1 M NaOH. The fields originated from the macroscopic surface currents (ionic and electronic), which appear due to corrosion potential differences that resulted from differences in electrolyte flow characteristics (velocity, direction, and turbulence). The measurements demonstrated SQUID capability of remote corrosion sensing across the integrated media consisting of gaseous and solid dielectrics, metal, and electrolyte. The results have shown the potential of magnetometry for practical corrosion detection in the restricted locations ("hidden" corrosion) where solution flow is applied.

Introduction

Significant efforts have been undertaken during the last two decades to introduce the SQUID (Superconducting QUantum Interference Device) magnetometry into corrosion science and engineering [1–22]. These efforts were directed to a challenging goal—development of a new technique, which would be capable of corrosion characterization noninvasively and remotely across dielectric medium. Nevertheless, the field remains to be at an early stage from both fundamental and practical points of view. There are very few studies aimed to demonstrate a relationship between the corrosion rate (j_{corr}) and the corresponding magnetic activity (B), if any, and no quantitative expressions between these parameters are known [12, 14, 17]. It is, therefore, not surprising that, so far, there is no a well-established magnetometric technique for practical characterization of corrosion defects.

The main difficulty in the basic magnetometric corrosion studies is the limited spatial resolution of the applied techniques (roughly 1 mm or greater), which is not sufficient to detect the magnetic activity of a single corrosion pit (with the size in the order of micrometers or even less). Due to statistically distributed corrosion pits and randomly orientated surface currents, the corroding surface could be magnetically silent on a macroscopic scale. Some progress suggests a SQUID microscope with improved spatial resolution, which was originally developed to measure biomagnetic and paleomagnetic fields [23]. The authors used submillimeter pickup coils from a low-temperature superconducting niobium wire coupled to the input circuit of a SQUID and achieved a spatial resolution of 250 μm with a magnetic field sensitivity of 850 fT/Hz$^{-1/2}$.

Another limitation lies in necessity to exclude natural or man-made magnetic noise, i.e., to perform the measurements in the specially shielded environment. To overcome this problem, attempts have been undertaken recently to apply the fluxgate gradiometer with two magnetic sensors [24].

Corrosion under hydrodynamic conditions is attractive for magnetometric investigations because in this case, generation of large-scale magnetic fields could be expected. An electrolyte stream due to variation in flow characteristics may cause appearance of the macroscopic domains with different corrosion potentials. The electromotive force between these domains may cause generation of associated electronic and ionic currents with a detectable magnetic component. The intrinsic magnetic activity of the liquid stream could be much less than that produced by corrosion process [22].

E. Juzeliūnas (✉)
Institute of Chemistry,
A. Goštauto 9,
2600 Vilnius, Lithuania
e-mail: ejuzel@ktl.mii.lt

Y. P. Ma · J. P. Wikswo
Department of Physics and Astronomy,
Vanderbilt University,
VU Station B 351807,
Nashville, TN 37235, USA

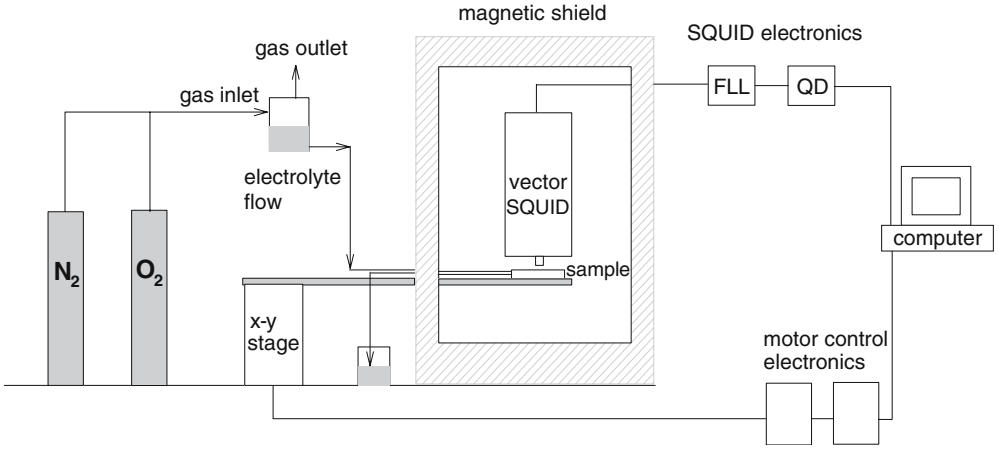

Fig. 1 The experimental setup of the magnetic imaging system under electrolyte flow conditions. The system consists of three-axis differential SQUID magnetometer with SQUID electronics, magnetic and rf shielding, x-y stage with motor control electronics, corrosion cell with sample inside the magnetic shield, electrolyte reservoir, gas supply to the electrolyte, and tubing and collecting vessel

In this study, hydrodynamically induced magnetic fields on an AA 2024 sample in NaOH and NaCl solutions were studied by SQUID magnetometry. Our goal was to demonstrate a capability of magnetometry to detect the corrosion activity remotely and across the multiphase system consisting of dielectrics (air and plastic) and electronic (metal) and ionic (electrolytes) conductors. The attempts were addressed to design the system, which simulated, to a certain extent, subjects of practical importance, for instance, subsurface corrosion in pipelines and aircraft structures.

Experimental

The experimental setup used (Fig. 1) was described in detail previously [17, 21, 22]. A high-resolution SQUID facility at Vanderbilt University was used. The SQUID magnetometer operating in liquid helium (Tristan Technologies) had a three-axis vector gradiometer system with a noise-cancelling reference SQUID. For each axis, a first-order differential gradiometer uses a pair of pickup coils (∅ 3 mm) separated vertically by a 30-mm baseline. The minimum operational distance between the z pickup coil and the dewar outside (room temperature) is 2.5 mm. The SQUID is controlled by a modified QD 5000 (Quantum Design) electronics that provided external feedback on four channels. A magnetic shield with dimensions of 1m×1.7m×2m consisted of two layers of Amumetal and two layers of aluminum, which provides the environment for the SQUID not higher than 12 fT/Hz$^{-1/2}$. A non-magnetic, high-speed x–y scanning stage driven by two stepper motors was placed outside the magnetic shield. It provided repeatable scans with positioning accuracy less than 0.1 mm.

Figures 2 and 3 show the design of corrosion cells and the AA 2024 samples. The cells were sandwiched from a plexiglas cell body, a rubber seal, and a plexiglas cover with an AA 2024 alloy sample underneath the cover or inside the cell. In some experiments, the plastic cover was replaced by an AA 2024 one, which represented the corroding sample and directly contacted the solution. The sample and the electrolyte compartment were of analogous shape. The width of the cell channels was 6, 10, and 20 mm, while the sample had the analogous dimensions of 2.5, 7, and 16 mm.

The corrosion cell was assembled using eight plastic screws. The assembled corrosion cell was connected to solution tubing and fixed on the x–y stage in the magnetic shield (always in the same position). The maximum distance between the SQUID dewar and the sample included the air gap between the dewar and the cell

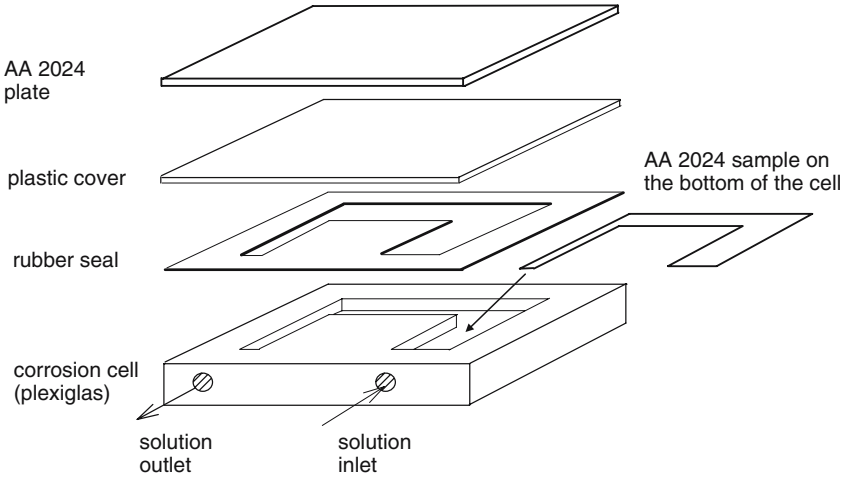

Fig. 2 The electrolyte flow cell with the AA 2024 sample inside, rubber seal, and plastic and AA 2024 covers. The distance between the SQUID dewar and the sample in the bottom of the cell was 12 mm, which included the air gap between the dewar and the cell (2 mm), the AA 2024 and plastic covers (1.5 and 0.8 mm), the rubber seal (0.8 mm), and the solution (7 mm). The cell enabled different electrolyte flow velocities due to the different width of the channel

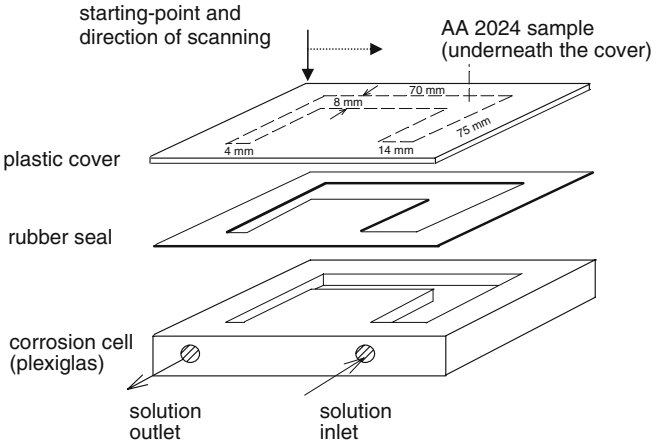

Fig. 3 The corrosion cell design with AA 2024 sample underneath the cover used in the SQUID magnetometry experiments

(2 mm), the AA 2024 and plastic covers (1.5 and 0.8 mm), the rubber seal (0.8 mm), and the solution (7 mm).

The samples were prepared from a commercial 1.5 mm thick AA 2024 aluminum alloy plate (McMaster Carr). In some experiments, to prevent electronic current flow along the sample, the latter was cut into 11 single sections of different size and geometry (sample configuration is shown in association with magnetic images).

The surface treatment before each experiment included sandpapering (grade 320 and 600), cleaning with filter paper, rinsing with acetone, drying under ambient conditions, washing with distilled water, and drying again.

The experiments were conducted at room temperature (20±2°C). The solutions were prepared from distilled water and analytical class purity reagents.

The SQUID data were processed using a program, which makes it possible to subtract one scanning data from another. For instance, to show electrolyte flow effect, the scanning data under no flow conditions were subtracted from those obtained under electrolyte flow.

The total magnetic activity of the scanned area was estimated by the spatially integrated magnetic activity (SIMA, nT mm^2) [13],

$$\mathrm{SIMA}(t_k, \Delta t) = \sum_{i}^{N_x} \sum_{j}^{N_y} \left[B_z\left(x_i, y_j, t_k, \Delta t\right) \right] \Delta x \, \Delta y \,, \qquad (1)$$

where Δx and Δy represent the distance between two consecutive pixels in the corresponding scan direction. The SIMA calculation takes the summations over all the pixels in the magnetic image, i.e., this value is proportional to the net magnetic activity of the sample during the surface scanning time.

Results and discussions

Figures 4, 5, 6, and 7 show the magnetic images (B_z component) obtained over the U-shaped sectional sample under no flow conditions (Figs. 4 and 5) and when different electrolyte flow velocities were applied (Figs. 6 and 7). The monolithic sample, which is shown in Fig. 2, was cut into single sections to prevent a current flow along the sample, which may appear due to different geometry and, consequently, different corrosion potentials of the end parts of the sample [17].

As depicted in the figures, the entire system under study comprised 11 single sections of different size and geometry, which were separated by 1 mm insulating gaps. The system exhibited in quiet solutions with relatively low magnetic activity SIMA$_z$=28 nT mm^2. The patterns also did not indicate any distinctive magnetic field distribution, which could be associated with configuration

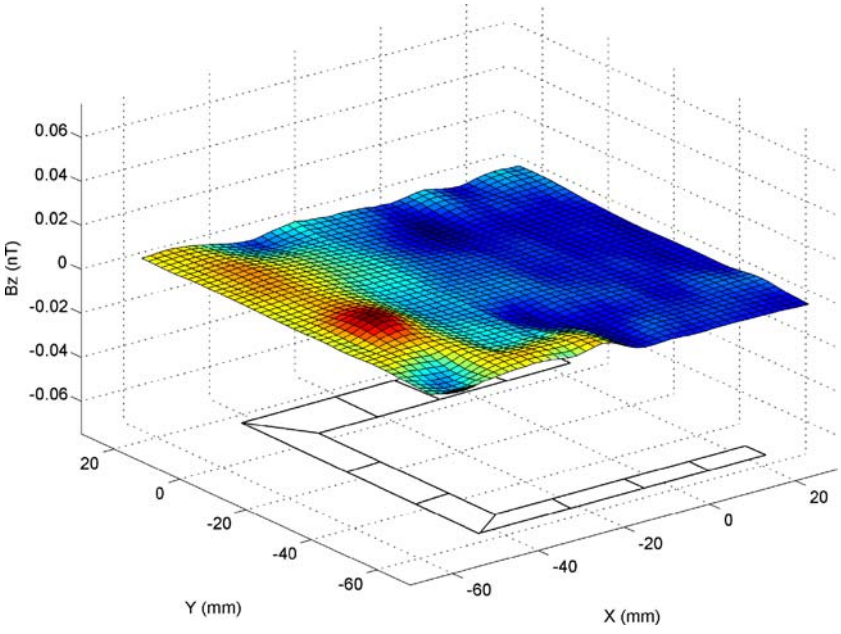

Fig. 4 Magnetic field image (B_z component) obtained for the U-shaped sectional sample in naturally aerated 3.5% NaCl solution under no-flow conditions. The cell design is shown in Fig. 3 and sample location is depicted below the magnetic image. Spatially integrated magnetic activity is SIMA=28 nT mm^2

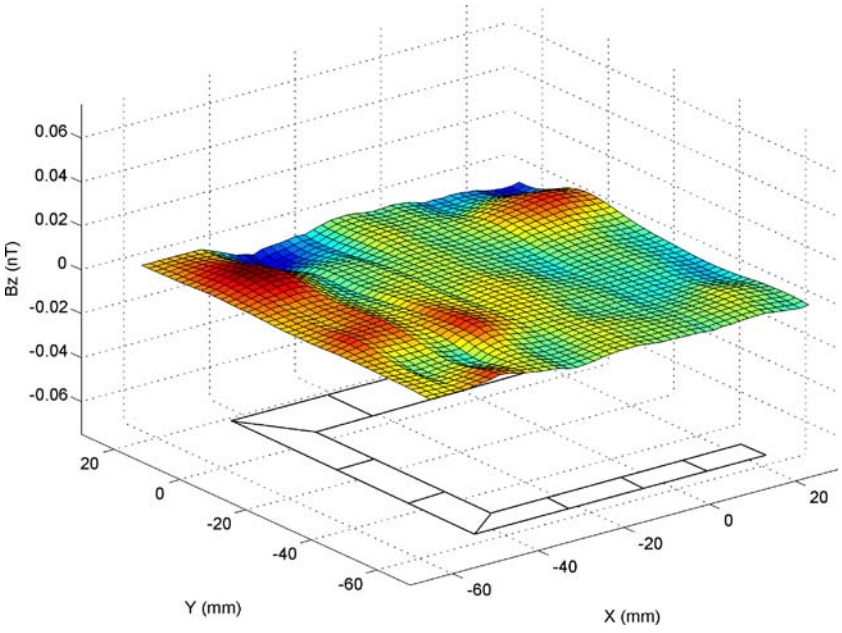

Fig. 5 Magnetic field image (B_z component) obtained for the U-shaped sectional sample in oxygen-saturated 3.5% NaCl solution under no-flow conditions. The cell design is shown in Fig. 3 and sample location is depicted below the magnetic image. Spatially integrated magnetic activity is SIMA=28 nT mm^2

of the single sections, entire system, or electrolyte channels. The magnetic activity did not respond to substantial increase in corrosivity of the environment, as evident from the equal activities determined in both naturally aerated and oxygen saturated solutions (Figs. 4 and 5). The corrosion rate of aluminum alloy in aerated solution was determined by the quartz crystal microbalance technique to be about five times lower compared to that in oxygenated solution [17].

Thus, the data obtained show that the system with respect to corrosion is magnetically silent. As the aluminum alloys corrode according to the so-called pitting mechanism, it may be concluded that pitting corrosion on a macroscopic scale (in our case millimeter or greater) is magnetically silent. The reason of this could be statistical distribution of the pits and randomly oriented surface currents (which cancel each other if they flow in opposite directions). It seems, therefore, that reports in the literature on detection of magnetic activity of pitting corrosion should be taken with some care [10, 11].

An increase in total magnetic activity with a characteristic spatial distribution of the magnetic field is evident when electrolyte flow is applied (Figs. 6 and 7). The activity zones are localized around the places of electrolyte inlet and outlet and especially around the corners, i.e., where solution turbulences are possible.

Another demonstration of hydrodynamically induced magnetic fields is given in Fig. 8. The data were obtained using the cell configuration and the monolithic U-shaped sample, which are shown in Fig. 2. It has been shown

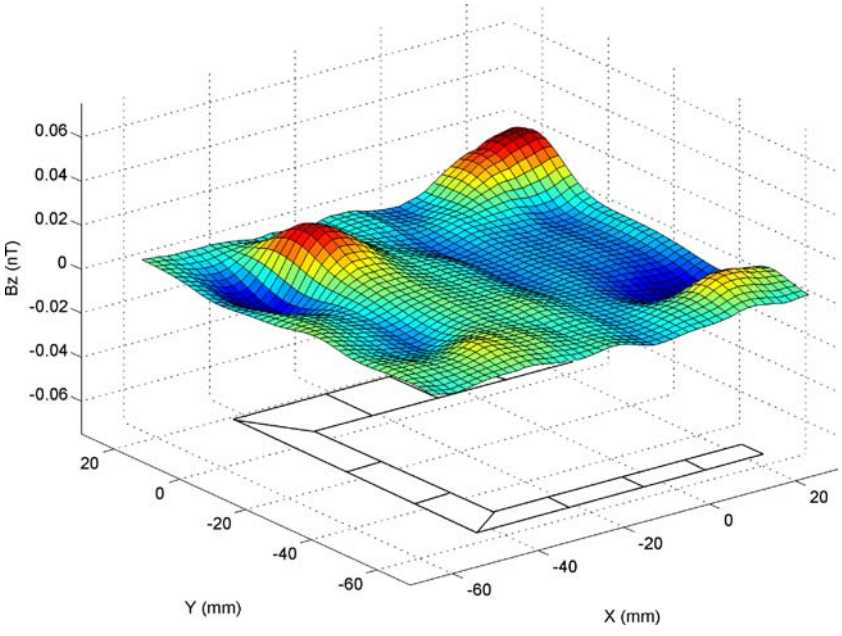

Fig. 6 Magnetic field image (B_z component) obtained for the U-shaped sectional sample in oxygen-saturated 3.5% NaCl solution under electrolyte flow 1 ml s^{-1}. The cell design is shown in Fig. 3 and sample location is depicted below the magnetic image. SIMA=46 nT mm^2

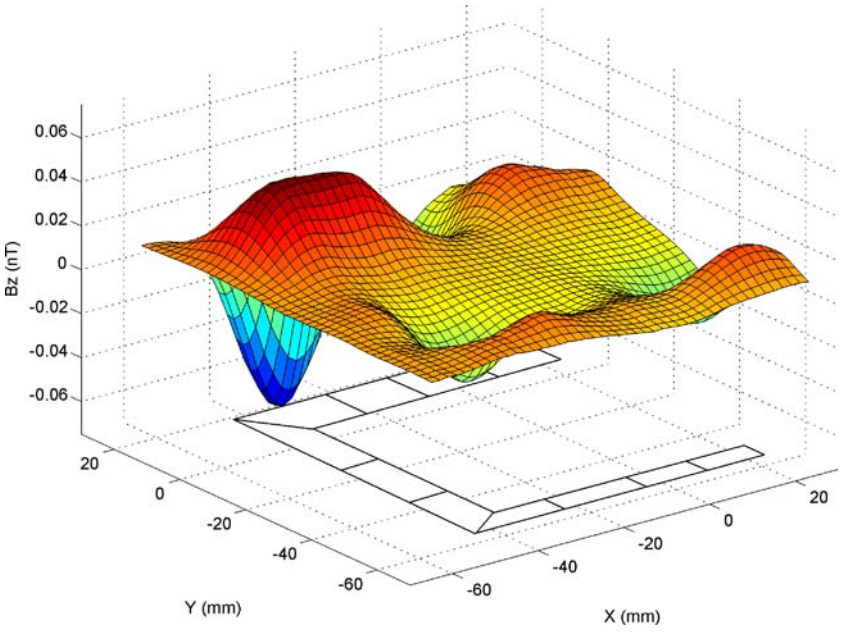

Fig. 7 Magnetic field image (B_z component) obtained for the U-shaped sectional sample in oxygen-saturated 3.5% NaCl solution under electrolyte flow velocity 8 ml s^{-1}. The cell design is shown in Fig. 3 and sample location is depicted below the magnetic image. SIMA=129 nT mm^2

previously that this sample exhibits a characteristic magnetic activity under no-flow conditions due to corrosion potential difference at the end parts of the sample [17]. To identify the flow effect, the magnetic flux image (x, y, and z components) first was obtained under flow conditions and then when solution flow was stopped. When processing, the data obtained in quiet solution were subtracted from those under flow conditions.

The data in Fig. 8 imply hydrodynamical generation of electronic current along the sample. The current is confirmed by the experiment in which an external current (j) passed through the sample with an electron flow direction from the narrow side to the wide one (Fig. 9). It is obvious that the dc images show resemblance to those obtained for the corroding sample (Fig. 8), with the main difference that the applied electron current flows to the end of the sample, whereas the corrosion current diminishes closer to the ends. It follows from the dc and SIMA values that the experimental system is characterized by the ratio dj/dB_z=1.4×10^{-7} A nT^{-1} mm^{-2}. According to this ratio, the hydrodynamically induced current in Fig. 8 is as high as j=23 μA. However, the electronic current in metal may be somewhat reduced by an ionic current in the solution, as discussed below. Nevertheless, the current value obtained is valuable for rough characterization of the process.

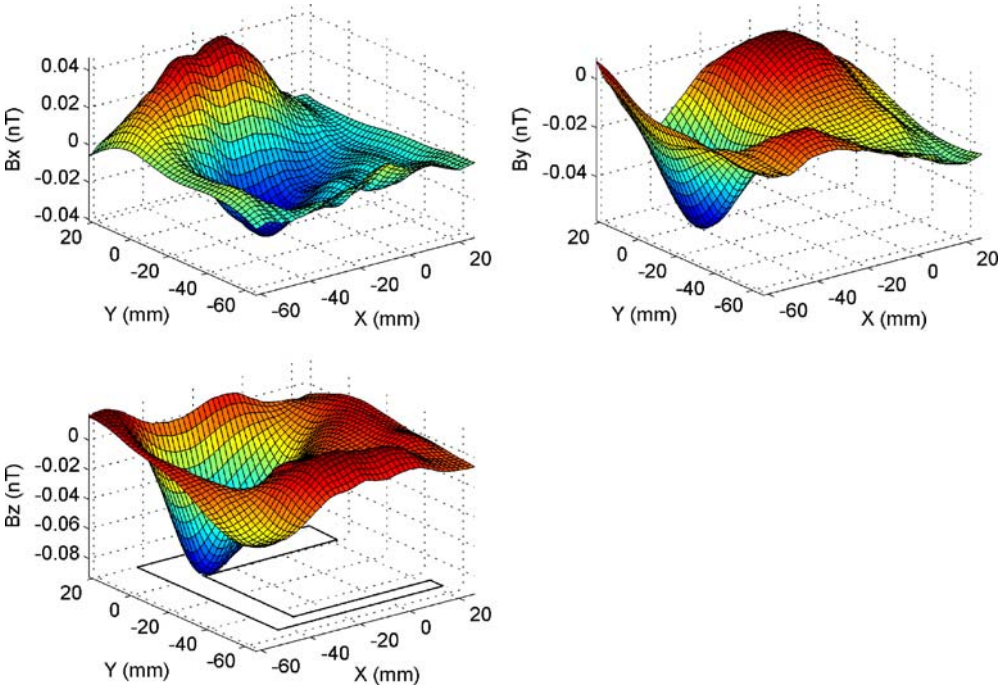

Fig. 8 Magnetic field images (x, y, and z components) obtained for a monolithic U-shaped AA 2024 sample in naturally aerated 3.5% NaCl solution at net flow velocity 7 ml s^{-1}. The scanning data obtained under no-flow conditions were subtracted from those obtained under flow conditions. The cell design and sample configuration is depicted in Fig. 2. Sample dimensions are given in Fig. 3. SIMA=166 nT mm^2

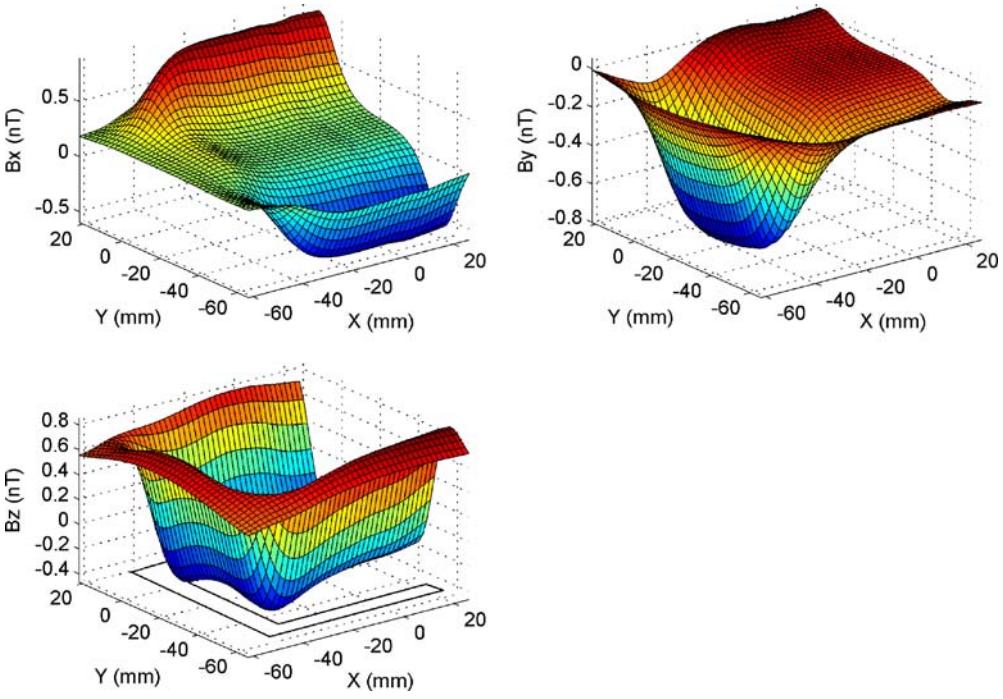

Fig. 9 Magnetic field images (x, y, and z components) obtained when dc (0.6 mA) was passed through the sample (Fig. 2 and as depicted below the image). The connecting wire contacts were glued to the ends of the sample using silver paint. Current polarity corresponded to electron flow from the narrow side of the sample to the broad one. SIMA=4,278 nT mm^2

The origin of j lies in the electromotive force, which emerges due to the corrosion potential (E_{corr}) gradient along the sample. It is commonly known that E_{corr} depends upon various factors, which may affect the rate of both the anodic and cathodic partial reactions of corrosion process. In our case, corrosion potential on different sides of the sample is different primarily because of different transport conditions of the oxidizing agent and products of the corrosion reaction. A solution stream with three different flow velocities and directions was applied in our experiment, and the flow velocities in different channels were in inverse proportion to their width (6, 10, and 20 mm). In addition, solution turbulences around the corners may contribute to the transport as well. According to the formal electrochemical kinetics, it is reasonable to expect that increase in electrolyte flow velocity will result in a positive shift of corrosion potential (acceleration of the partial cathodic reaction of corrosion process). Thus, the anodic reaction of the corrosion process

$$2Al + 3H_2O \rightarrow Al_2O_3 + 6H^+ + 6e \quad (2)$$

will be promoted on the narrow side of the sample, while the cathodic reaction

$$O_2 + 2H_2O + 4e \rightarrow 4OH^- \quad (3)$$

will predominate on the broad side. Accordingly, the narrow side will act as an anode and the broad side as a cathode. The electrons produced in reaction found in Eq. 2 will move from the narrow side to the broad one, where they will be accepted by reaction found in Eq. 3.

The corrosion process is associated also with generation of ionic currents, which are due to the release of protons by Eq. 2 and hydroxyl ions by Eq. 3. Both the electronic and the ionic currents represent a closed contour, which extends in metal and solution phases. It means that the electronic currents in the metal has an opposite direction to that of the ionic currents in the solution and, therefore, the magnetic fields induced by electronic currents are oppositely directed to that induced by the ionic currents. However, both magnetic fields do not cancel each other because of different spatial distribution: the ionic currents are distributed in the large volume of the solution above the sample, while the electronic currents are localized within a much thinner sample. Nevertheless, one can expect that the ionic currents reduce the strength of the observed magnetic field as compared to that produced by the electronic currents alone. This should be taken into account when interpreting the discussed-above current value j=23 μA calculated for the data in Fig. 8.

The magnetic activity of the solution stream itself in metal-free cell was studied in detail previously [22]. Although some magnetic activity of the stream was detected, it was much less than the activity resulted from metal–solution interaction. The magnetic images of the solution stream were of randomly distributed character; they did not indicate the geometry of the flow channels. The intrinsic magnetic activity was explained by an interaction between the liquid flow and the walls of the plexiglas channel, probably, by the streaming potentials due to the relative motion between a charged surface and the solution. No indications of magnetic activity of aluminum corrosion products were found.

The cell design used in Fig. 10 allowed certain discrimination between the ionic and the electronic currents. In these measurements, the cell depicted in Fig. 2 was modified so that no metal sample inside the cell was used and the plastic cover was replaced by the AA

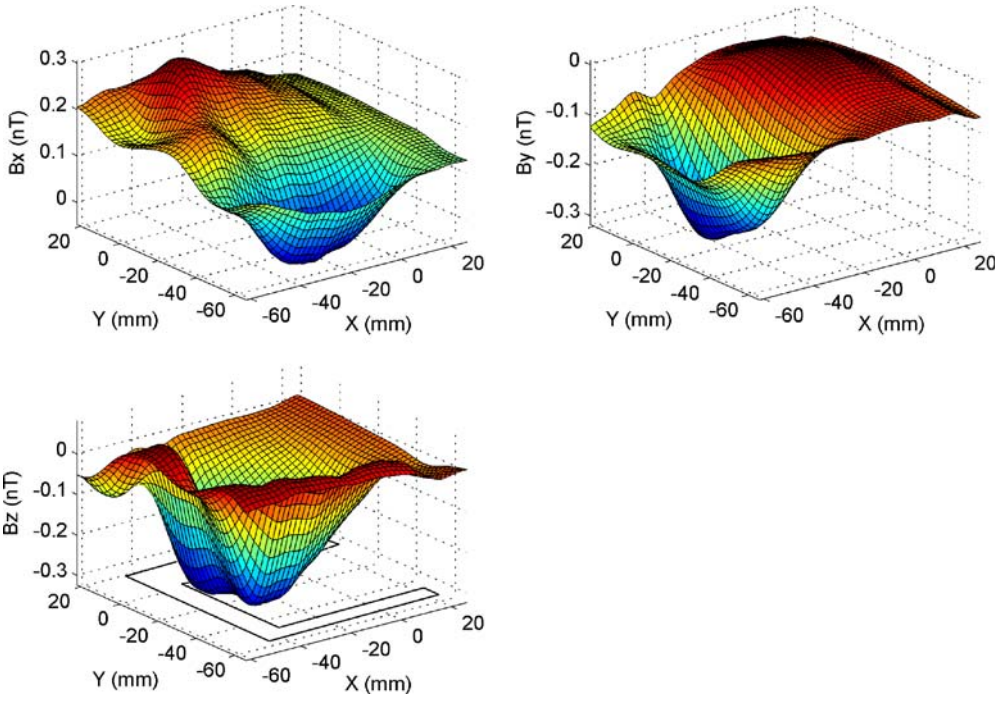

Fig. 10 Magnetic field images (x, y, and z components) obtained using modified cell in Fig. 2 (only the AA 2024 cover, no plastic cover and no AA 2024 sample inside the cell). The electrolyte was 0.1 M NaOH and flow velocity was 1.5 ml s^{-1}. The dotted lines denote metal/solution interface. The scanning data obtained under no-flow conditions were subtracted from those obtained under flow conditions. SIMA=827 nT mm^2

2024 one. The latter also played the role of U-shaped corroding sample, as the cover directly contacted the solution channel. Due to corrosion, both electronic and ionic currents may appear at the metal/solution interface, whereas only electronic currents on the rest of the surface are possible. For instance, the electron flow between the both sides of the U-shaped corroding area is possible due to the electrochemical potential difference.

The magnetic images in Fig. 10 clearly indicate the current along the corroding area as evident from the similarity of the data with those obtained when applying the external current (Fig. 9). The current is produced by the electromotive force due to the corrosion potential difference at the end parts of the U-shaped area and generation of electronic current associated with the ionic one along the metal/solution interface. It is difficult to decide as far as it concerns the fields produced by the electronic currents on the rest of surface, if any. It is obvious, however, that induction of the magnetic fields is strongly favored where the ionic currents are possible.

Conclusions

A U-shaped aluminum alloy (AA 2024) sample, which comprised 11 single sections of different size and geometry, did not exhibit a distinctive magnetic activity during corrosion in a naturally aerated 3.5% NaCl solution. The total magnetic activity of the sample did not respond to corrosion enhancement by solution saturation with oxygen. These data have shown that pitting corrosion might be magnetically silent on a macroscopic scale (millimeter or greater) due to statistical distribution of corrosion pits and randomly oriented surface currents.

Macroscale magnetic fields were induced hydrodynamically on the sectional sample as well as on the monolithic one. The highest magnetic activity on the sectional sample was detected around the places where solution turbulences were possible. The magnetic field patterns indicated a current flow along the monolithic sample; the current configuration was confirmed by experiments with an external dc.

The hydrodynamic induction of magnetic fields is owing to the corrosion potential gradients, which in turn are due to differences in transport conditions of the oxidizing agents and the corrosion products. The differences cause appearance of associated electronic–ionic currents, which represent a closed contour extending in both metal and solution phases. The experiment, in which differentiation between the electronic and the electronic–ionic currents was possible, indicated that magnetic field generation by electronic–ionic currents was prevailing when compared to electronic currents alone, if any.

The SQUID magnetometer was demonstrated to be capable of remote sensing of corrosion under hydrodynamic conditions across the multiphase system “air–plastic–metal/solution”.

Acknowledgement E.J. acknowledges the Council for International Exchange of Scholars (Washington, DC) for a Fulbright research fellowship.

References

1. Bellingham JG, MacVicar MLA, Nisenoff M, Searson PC (1986) J Electrochem Soc 133:1753
2. Bellingham JG, MacVicar MLA, Nisenoff M (1987) IEEE Trans Magn 23:477

3. Misra M, Lordi S, MacVicar MLA (1991) IEEE Trans Magn 27:3245
4. Hibbs AD (1992) IEEE Trans Magn 139:2447
5. Weinstock H (1991) IEEE Trans Magn 27:3231
6. Li D, Ma YP, Flanagan WF, Lichter BD, Wikswo JP Jr (1995) JOM-J Min Metall 47:36
7. Li D, Ma YP, Flanagan WF, Lichter BD, Wikswo JP Jr (1996) Corrosion 52:219
8. Li D, Ma YP, Flanagan WF, Lichter BD, Wikswo JP Jr (1997) Corrosion 53:93
9. Matthews R, Kumar S, Taussig DA, Whitecotton BR, Koch RH, Rozen JR, Woeltgens P (1997) Inst Phys Conf Ser 1–2:767
10. Richter H, Knecht A (1997) Materialprüfung 39:390
11. Andrieu C, Dalard F, Rameau JJ, Alcouffe F, Reboul M (1998) J Mater Sci 33:3177
12. Juzeliunas E, Hinken JH (1999) J Electroanal Chem 477:171
13. Skennerton G, Abedi A, Kelly RG, Wikswo JP Jr (2000) J Corros Sci Eng 3:2 (at http://www.cp.umist.ac.uk/JCSE/)
14. Juzeliunas E, Samuleviciene M, Sudavicius A, Hinken JH (2000) Electrochem Solid-State Lett 3:24
15. Juzeliûnas E, Hinken J (2000) Electrochim Acta 45:3453
16. Lima EA, Bruno AC (2001) IEEE Trans Appl Supercond 11:1299
17. Ma YP, Wikswo JP, Samuleviciene M, Leinartas K, Juzeliunas E (2002) J Phys Chem B 106:12549
18. Yashiro H, Yoshizawa M, Kumagai N, Hinken JH (2002) J Electrochem Soc 149:B65
19. Menzel K, Krause H-J, Sawade G (2002) Mater Corros 53:417
20. Carr C, Graham D, Macfarlane JC, Donaldson GB (2003) Supercond Sci Technol 16:1387
21. Juzeliûnas E, Ma YP, Wikswo JP (2004) J Solid State Electrochem 8:435
22. Ma YP, Wikswo JP, Juzeliûnas E (2005) Corros Sci 47/3:621
23. Baudenbacher F, Peters NT, Wikswo JP Jr (2002) Rev Sci Instrum 73:1247
24. Wrobel H, Tavrin Y, Wenk M, Hinken JH at: http://www.elektrotechnik.hs-magdeburg.de